Payri, R.; Bracho Leon, G.; Marti-Aldaravi, P.; Marco-Gimeno, J. (2020). Computational Study of Urea-Water Solution Sprays for the Analysis of the Injection Process in SCR-like Conditions. Industrial & Engineering Chemistry Research. 59(41):18659-18673. https://doi.org/10.1021/acs.iecr.0c02494

Computational study of urea-water solution sprays for the analysis of the injection process in SCR-like conditions

Raúl Payri, Gabriela Bracho, Pedro Martí-Aldaraví,* and Javier Marco-Gimeno

CMT - Motores Térmicos, Universitat Politècnica de València, Valencia, 46022, Spain

E-mail: pedmar15@mot.upv.es

Abstract

Exhaust after-treatment devices for NOx reduction have become mandatory for achieving the strict diesel emission standards. The Selective Catalytic Reduction (SCR) method has proven to be efficient in this task. Nonetheless, in order to improve the efficiency of the system, the Urea-Water Solution (UWS) injection process needs to be properly characterized due to the limited geometry of the exhaust line and its flow conditions. In combination with the experimental analysis into the system in a dedicated test rig, Computational Fluid Dynamics (CFD) studies provide better insight of the physical phenomena. Therefore, the main objective of this investigation is to achieve validated droplet size and velocity distributions in the simulation similar when compared to experiments. Three different positions along the spray are evaluated for that. The methodology adopted includes an Eulerian-Lagrangian approach to study the UWS spray. The results obtained with it show a proper experimental validation as well as the Sauter Mean Diameter distribution for the conditions tested. The proposed model accurately reproduces the main spray characteristics for different injection pressures and ambient conditions. Thus, the main conclusions obtained sum up in a good methodology for predicting UWS sprays in SCR-like conditions.

Introduction

Due to the increasing awareness of the impact on health and on environment of the polluting emissions of Internal Combustion Engines (ICE), novel reduction systems are being introduced. In the case of Diesel engines, NOx emissions are one of the main problems.[1,2] Selective Catalytic Reduction (SCR) has been determined to be one of the most efficient deNOx methodologies.[3–7] The technology consists of an injection event of Urea Water Solution (UWS) which transforms into ammonia (NH_3) via evaporation, thermolysis and hydrolysis of the spray.[8] The ammonia mixes with the exhaust stream, entering into the SCR device transforming the incoming products into H_2O and N_2.

Proper understanding of the UWS dosing system and the spray development has become of high importance because inadequate injection processes could lead into formation of Urea deposits in the engine exhaust line that could result in increasing line pressure drop, blockage of the pipe and low NOx conversion.[9,10] Moreover, the need of properly mixing and evaporating UWS in small distances plus its decomposition into NH_3 leaves very little time for the process prior to SCR to be completed.[11,12]

In the published literature there are some studies about the UWS plume characteristics to help the understanding of the spray mixing of the UWS. Work has been done to assess the spray impingement process into the liner exhaust walls[13] and its comparison against PIV measurements at different cross flow velocities. Droplet size distribution was also obtained and validated against PDA and Mie scattering on a 45° wall-tilted injector.[14] The control volume was computationally recreated, being the original geometry simplified into a rectangular channel of $80\,mm^2 \times 80\,mm^2$ on a 1M hexahedral cell region and tested with RANS methods, specifically the $k-\varepsilon$ RNG model for the closure of the transport equations and standard wall functions. The gas density, viscosity and specific heat were computed with the ideal law, Sutherland law and Cp polynomial respectively, while the liquid phase was introduced in a Lagrangian way. Both previous works focused on wall-impingement phenomena, and showed certain deviations while matching the experimental and computational diameter

distributions. Buoyancy was found to have little effect on the spray characteristics. On the contrary, droplet coalescence had an impact on the results accuracy. Vortexes were created on the spray core which tended to decrease with higher cross mass flows. Global characteristics of the spray have been studied by Van Vuuren et al.,[15,16] analysing the effect of the exhaust flow and spray temperature, showing dependencies of the spray morphology on the injected fluid temperature up to flash boiling conditions, showing an expansion of the spray and an improvement on the atomization, but not on the gas flow temperature. Other studies have been performed substituting the urea by water when the deposits are not the focus of the study, due to its similar properties.[17] It showed that except for the jet inclination angle, the rest of spray characteristics were affected by the change of fluid, showing higher Weber and Ohnesorge numbers for water as well as lower nozzle exit velocities. Additionally, with UWS fluid the liquid length tended to shorter distances with increasing injection pressures while for water the opposite tendency was found, suggesting that this replacement moves the breakup regime from first wind induced to the second wind induced. Additional studies have been made by Rogóż et al.[18] which introduced a two-zone spray approach for characterizing the Urea spray and wall impingement. The droplet size distribution coming from experimental results was introduced as boundary condition into the model and the validation with the experimental data was done in terms of spray penetration. The approach showed relevant results when it comes to deposition of the Urea into the walls, as if the two-zone approach was used, higher wall film formation which suggests more non-evaporated liquid at the walls compared to the traditional approach, as well as a worse film distribution on the walls. Other metrics used such as the Ammonia Uniformity Index seemed to be little affected by the spray model used, whether the standard or the two-zone approach. On the other hand, Bebe et al.[19] injected water into still air, and calibrated the computational simulation based on experimental results. As a results, they remarked the importance of a proper calibration of the main spray parameters such as cone angle and penetration to faithfully represent the water spray, and highlighted the dependency of the droplet size distribution

on the characteristic diameter of the spray.

The objective of this study is to create a methodology capable of predicting droplet size distribution and velocities in exhaust-like conditions for different injection pressures and exhaust gas mass flow. The computation of the desired spray characteristics are performed at three different positions, one near the nozzle exit and two in the already developed spray. Computational results are to be compared against measurements on a test rig capable of reproducing the desired flow conditions.

The document is divided into four sections as follows: an introduction (this section) where an state of the art is presented, the experimental results, where it is explained how the data coming from the test rig is obtained. In the computational set-up section the model used is detailed, followed by the results which includes the model validation and a pressure and cross mass flow sensitivity study, and ending up with the main conclusions obtained.

Experimental Dataset

The designed test rig is capable of reproducing exhaust-like conditions with air flow rate up to 400 kg/h and temperatures up to 400 °C thanks to a 15 kW electric heater from LEISTER. Both conditions can not be achieved simultaneously, as the maximum temperature at a flow rate of 400 kg/h is about 250 °C, and at 40 kg/h, the heater can achieve up to 450 °C. Temperature is measured with a K-Type Thermocouple and controlled with a PID. For the experimental campaign, a flow rate of 40 kg/h is used, which implies an air flow rate below typical light duty diesel engines.[20] The air is introduced into the system by means of a blower, and the air flow rate is controlled before reaching the electric heater with a hot wire flow rate sensor. This flow condition has been tested at 180 °C and 350 °C, but for this work, only the higher temperature results are shown as it represents a more realistic SCR condition. This temperature is achieved with an electric heater which is located prior to the injection chamber, and it is measured with a K Type Thermocouple and controlled with a PID. The

injector is placed with an angle of 90° with respect to the incoming flow. A schematic view of the rig is included in Figure 1. A complete explanation of the experimental set-up and

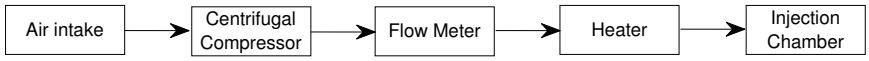

Figure 1: High flow and temperature installation.[21]

data processing is included in the work of Payri et al.[21,22] The injector corresponds to a Bosch dosing module, composed of 3 holes with diameter of 145 µm each, which corresponds to the narrower circular section of the nozzle diameter. The injection chamber consists on a parallelogram of size 70 mm × 70 mm × 180 mm (width, height and length respectively). The injection event is controlled with an electric signal which applies voltage to the injectors solenoid. The tested injection pressures are 4, 6 and 8 bar, which are typical working conditions for the used injector. The complete set of working conditions of the test rig is included in Table 1. The technique used is diffused back-light illumination (DBI), a light of a LED passes through the spray towards a receiving camera.[23] The liquid phase blocks the light coming from the source, and the camera receives light where there is no spray, and shadow where there is liquid. The high speed camera is capable of obtaining a resolution of 40.2 pix/mm, and it is used with an acquisition frequency of 150 kfps, and a depth of field of 1 mm. The obtained images underwent an image correction procedure, spray boundary detection by binarizing the images, image noise mitigation and finally penetration and spray angle computation for obtaining macroscopic features[22] such as spray angle and penetration. For the droplet diameters and velocities, the images follow background removal, binarization, droplet identification and then droplet characteristics calculation. Also the velocity is calculated with a frame to frame droplet search algorithm to calculate the speed of the droplets.[21]

The data has been obtained at three different windows of interest, P1, P2 and P3, as shown in Figure 2. The validation study of the computational results will be done in the same three windows.

Table 1: Experimental conditions.

Parameter	Value
Air flow rate	$40\,\mathrm{kg\,h^{-1}}$
Air Temperature	350 °C
Injected Fluid	AdBlue
Injection Pressure	4,6,8 bar
Injector Excitation Time	5000 ms

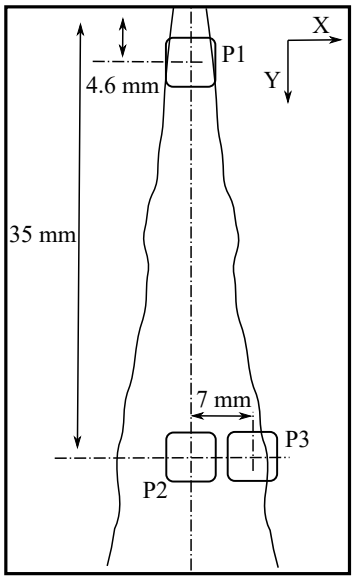

Figure 2: Definition of the location of the windows used for the droplet size and velocity calculation.[21]

Computational Set-up

The geometry and numerical set-up used for this research is described in this section. CFD simulations are performed using the commercial CFD software CONVERGE v3.0. The simulated geometry consists of a section of the test rig where the UWS dosing unit is located, and has been simplified (in comparison to the test rig chamber) into a cube of 70 mm × 70 mm × 70 mm in order to reduce the cell number and speed up the computational campaign without affecting the accuracy of the model. The simplified is as accurate as the original due to the injection droplet splashing directly into the lower chamber wall instead of going into the X direction. The injector is located at the ceiling center of the flow passage. Its orientation is normal to the ceiling wall, which is 90° with respect to the incoming cross-flow which flows in the positive X-axis direction. A comparison of the test rig geometry and the CFD geometry is included in Figure 3. The mesh consisted in hexahedrical cells of 1.5 mm × 1.5 mm × 1.5 mm as suggested for low pressure sprays.[14] Adaptive mesh refinement (AMR) was introduced to refine elements that introduced a significant velocity gradient, with two levels of refinement, which introduces elements of half the base size for each refinement level. The AMR is set to trigger on cells whose sub-grid velocity is above 1 m s^{-1}. A snapshot of a mesh cut is introduced in Figure 4 which shows the difference between the mesh size and the element size reduction due to the AMR. Initially, a grid independence study was performed. Base size was decreased from 1.5 mm to 0.75 mm and increased to 3 mm. Results of droplet size and velocity distributions of this study are displayed in Figure 5. There are not significant differences in velocity distributions, but the Probability Density Function (PDF) of droplet diameter is slightly modified. Therefore, the finest mesh is selected for all the simulations of this work (finer meshes showed negligible differences).

Reynolds-Averaged Navier-Stokes (RANS) k-ε RNG for turbulence modeling has been selected due to literature usage in low pressure injection applications.[13,14] Cross flow is initialized according to the experimental flow rate and boundary conditions are set up as a

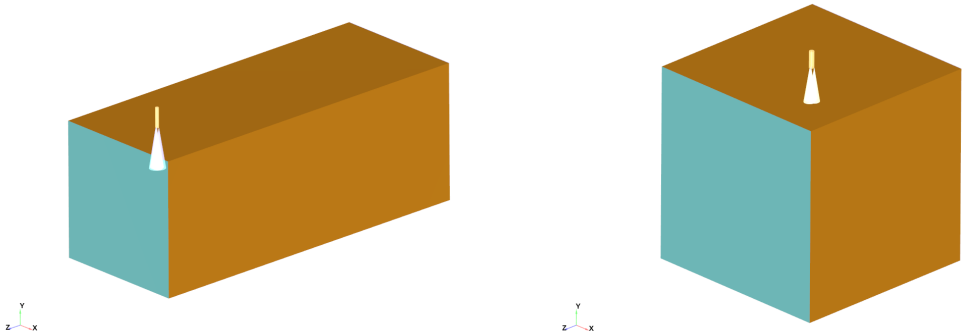

(a) Original geometry (b) Simplified geometry

Figure 3: Comparison between the original injection chamber and the modeled geometry introduced in the CFD simulations.

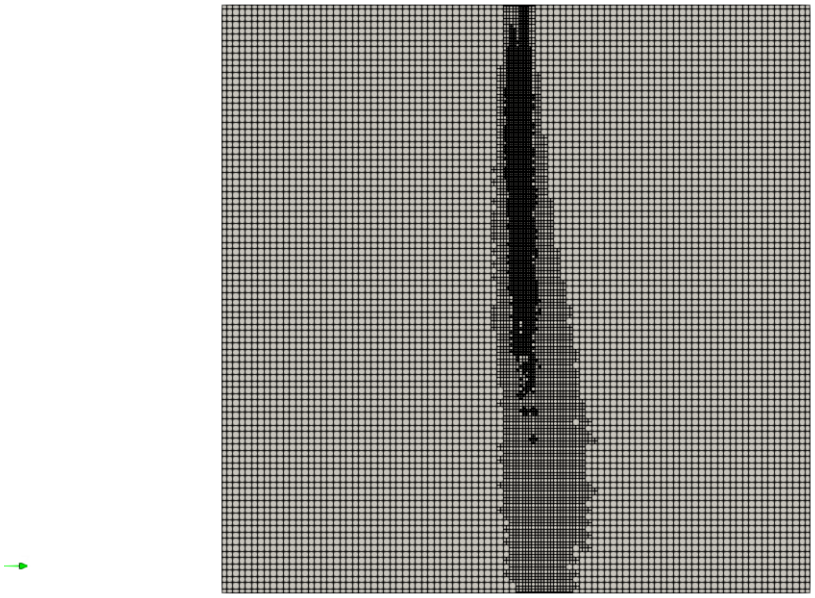

Figure 4: Effect of the AMR embedding in the volume mesh.

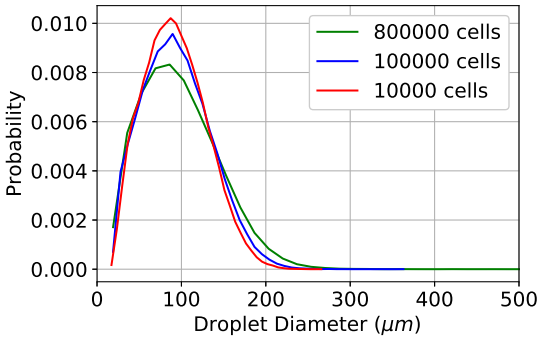

(a) Droplet Diameter

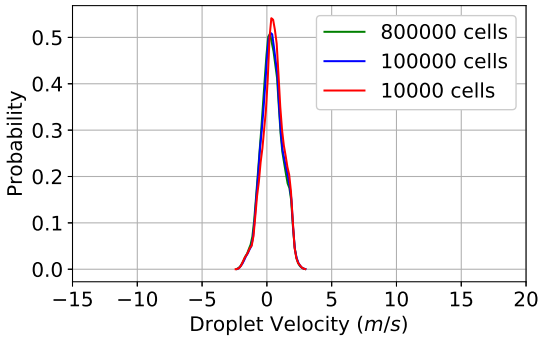

(b) X-Velocity

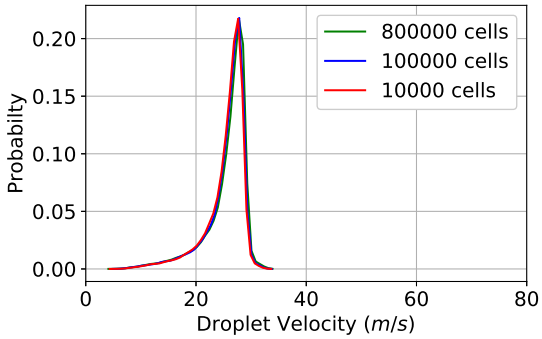

(c) Y-Velocity

Figure 5: Probability distributions of Droplet Diameter and Velocities for different meshes for an injection pressure of 6 bar, air at 350 °C and an air mass flow rate of 40 kg h^{-1}.

velocity-driven flow, by specifying a mass flow inlet on the domain inlet. Walls are set as adiabatic, no-slip surfaces. Complete set of boundary conditions are summed up in Table 3, including the Energizing Time, being the time in which electric current goes through the injector's solenoid, controlling the duration of the fluid injection into the domain. The main effect of this factor in real operating conditions is that it controls the total injected amount (the longer the time, the higher the injected amount). For the experiments and simulations, a long energizing time ensures stabilized injection conditions (with no influence of the injector needle opening or closing). As it is not intended to assess the behavior of the liquid phase into the walls, droplets vanish once a wall is reached. The injected liquid phase is commercial AdBlue solution (67.5% H_2O, 32.5% $CO(NH_2)_2$),[24] the same compound used in the experiments. Injection pressure is calculated based on total injected mass and the duration of the injection event (both specified), obtained from an experimental characterization of the dosing module to be used with the formulas provided in Equation 1 and Equation 2. Discharge coefficient has been calculated to match the experimental injection pressure.

$$V = \frac{m}{\rho \; A \; dt} \tag{1}$$

$$P_{inj} = \frac{1}{2}\rho\frac{V^2}{C_d^2} \tag{2}$$

AdBlue droplets are introduced with parcels, which contain sets of droplets with same characteristics. The position and the evolution of the parcel characteristics are followed during the whole domain. Their diameters are calculated in each simulation time step according to evaporation and droplet breakup or coalescence. The number of parcels to properly predict the spray characterization has been selected per bibliography as a reference value of $1.5 \times 10^{-10}\,\mathrm{kg\,parcel^{-1}}$.[25] An additional study of the dependence of the solution on the number of parcels has been also done, whose results are included in Figure 6, concluding in 75×10^3 parcels per nozzle, which show the same behavior in terms of velocity and droplet distributions as simulations with higher number of introduced parcels, but with a lower

computational cost. As a Lagrangian-Eulerian treatment, the liquid phase needs to be introduced as an already created droplet size distribution. It will be part of the study at a later stage of the document. When it comes to the atomization, Kevin-Helmholtz/Rayleigh-Taylor (KH-RT)[26] has been applied, although this kind of droplet breakup is not expected to happen due to the low velocities and therefore low Weber number. KH-RT constants values are set as default and shown in Table 2. No-Time-Counter (NTC) collision model[27] has been activated for predicting collisions between droplets, along with the Spherical Drop drag model of the droplets. Evaporation model has been activated to predict droplet vaporization, and Chiang sub-model has been chosen.[28] The injection rate-shape (Figure 7) is also set to be able to faithfully reproduce the transient parts of the injection event and possible consequences of the needle dynamics. These rate-of-injection curves are obtained from experimental results and processed to remove noise-related oscillations.[29,30] The test matrix to be simulated consists on three different injection pressures. A further study will include as well an increase in the air mass flow rate.

Table 2: KH-RT model constants used in the simulations.

Parameter	Value
Fraction of injected mass/parcel	0.05
Shed mass constant	1.0
Model size constant	0.6
Model velocity constant	0.188
Model breakup time constant	7.0

The complete control volume is initialized with air as the gas media and a velocity of $1.85\,\mathrm{m\,s^{-1}}$ in the X-direction that corresponds to $40\,\mathrm{kg\,h^{-1}}$ of air mass flow, ambient pressure and 350 °C. Simulation first iterations are performed only with gas phase for a boundary layer formation and the gas phase to reach a steady condition which is assessed by the evolution of the average domain pressure and velocity evolution over time. It is reached after 5 ms, when the first liquid parcels are introduced into the domain.

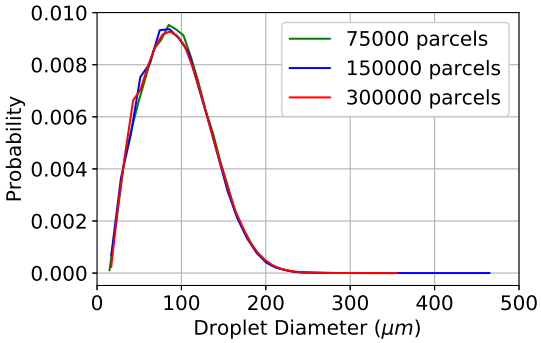

(a) Droplet Diameter

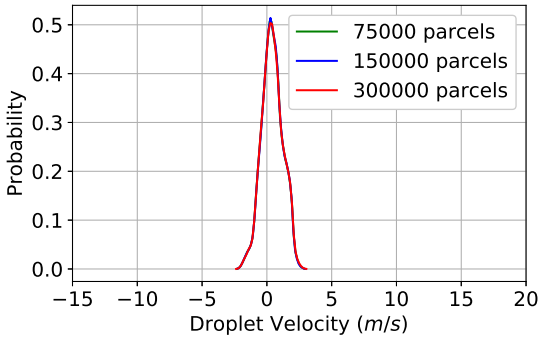

(b) X-Velocity

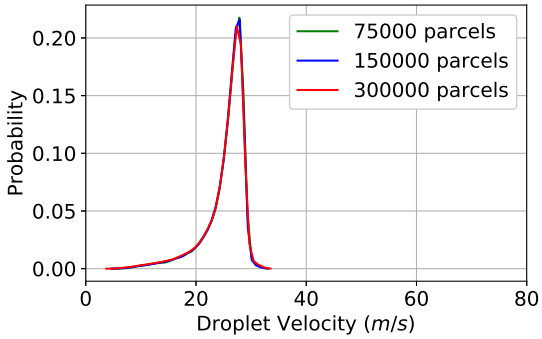

(c) Y-Velocity

Figure 6: Probability distributions of Droplet Diameter and Velocities for different number of parcels injected for an injection pressure of 6 bar, air at 350 °C and an air mass flow rate of 40 kg h^{-1}.

Table 3: Injection conditions.

Parameter	Value
Flow rate	40 kg/h
Injection pressure	4-6-8 bar
Injection temperature	300 K
Outlet pressure	1 bar
Temperature	180-350 °C
Energizing time	5000 µs

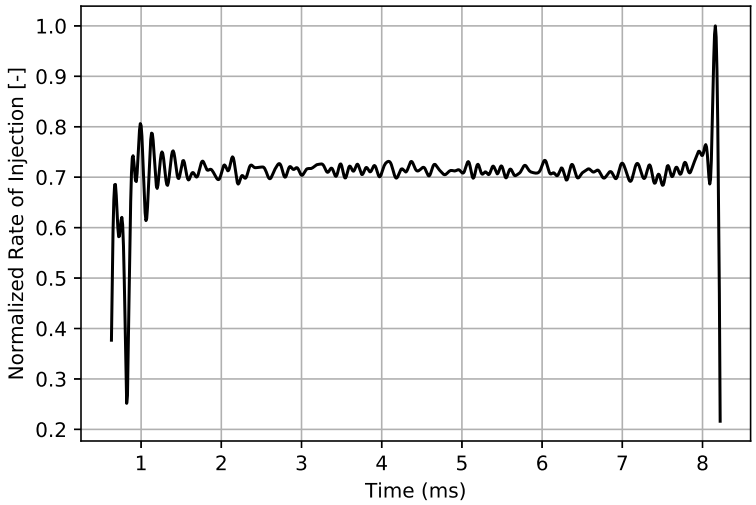

Figure 7: Example of a normalized ROI profile for 6 bar, 5000 µs of Energizing Time (ET).

Results and discussion

Droplet size distribution

The atomization of the jet is of great importance for the later development of the spray. If the injected fluid jet breaks apart into smaller droplets, and these droplets tend to break into even smaller droplets, evaporation would take place in a shorter time due to the smaller exposed area, accelerating the Urea decomposition mechanisms.[31] Although the KH-RT model should take into account both the primary and secondary atomization phenomena, it fails to predict the primary atomization event due to the low Weber number conditions.[32] On the other side, the injected droplets show a Weber number below 12, which happens to be the threshold for the secondary atomization to take place.[33] Figure 8 helps to confirm the lack of secondary atomization. It represents all the droplets detected for a simulation performed at 6 bar of injection pressure in the previous domain on an Ohnesorge(Oh)-Reynolds(Re) chart, that measures the importance of gravitational, inertial, viscous and surface tension forces. Reynolds number stands for the relationship between the inertial and viscous forces, while the Ohnesorge number relates the viscous forces with the surface tension forces. All the droplets fall in the region of Rayleigh breakup, induced by the surface tension forces, first

and second wind induced regimes, caused by the relative velocity between the jet and the gas, but none of them happen to be in the atomization region. Therefore, the injected droplets will most likely remain in their original size in the whole injection. For that, several Rosin-Rammler droplet distributions have been studied to see which one best fits the experimental results in the fields of view presented in Figure 2.

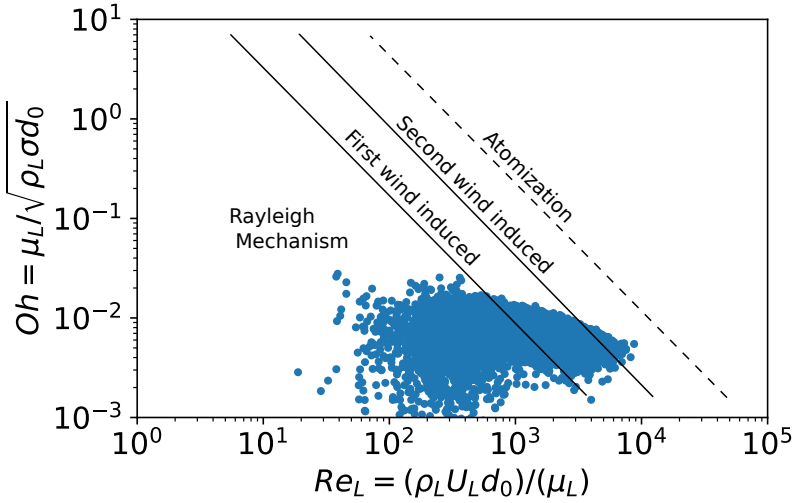

Figure 8: UWS droplets breakup mechanism in Re-Oh chart[33] for a 6 bar injection pressure, 350 °C of air and 40 kg/h of air mass flow rate.

This droplet distribution is driven by two parameters, the scale parameter, d_0, and the shape parameter, k,[13] as shown in Equation 3.

$$1 - Y = \exp\left[-\left(\frac{D}{d_0}\right)^k\right] \tag{3}$$

Shape parameter controls how flat or spread the probability distribution of the droplet size is. A shape parameter of k = 3 has been used after iterating this parameter and comparing experimental and computational curves to see which shape agreed best within the value range suggested by Lefebvre.[33] The values of the characteristic diameter, d_0, are chosen according to the value of the nozzle throat diameter, $d_n = 145\,\mu m$, simulating cases with d_n, $0.6d_n$, $0.5d_n$ and $0.3d_n$. These values correspond to geometrical data from inside the UWS

injector: the nozzle diameter (d_n), the distance between the needle head and the needle seat, ($0.6d_n$), half the nozzle diameter ($0.5d_n$), and the narrowest gap inside the injector respectively ($0.3d_n$). By seeing which parameter fits best, it is possible to assess which part of the geometry sizes the spray characteristics.

In order to obtain the most appropriate scale parameter, all three cases have been compared with experimental data in terms of droplet diameter, velocity in the cross flow direction (X-direction) and in the injector axis direction (Y-direction). Results are shown in Figure 9. It shows the probability distribution of the droplet diameters and the velocity component in each of the directions of interest, the injector axis (Y-direction) and the cross-air flow axis (X-direction), for the three regions of interest depicted in Figure 2 and for all the particles that go through these windows during the stabilized region of the injection event (2 ms - 7 ms).

From the cases simulated, $0.5d_n$ shows the best agreement in terms of droplet size diameter for P1 (Figure 9a), but for P2 and P3, $0.3d_n$ matches better the experimental results (Figure 9d and Figure 9g). The reason behind it is that there is a significant change in the PDF of the experimental results from P1 to P2, as the jet primary breakup process is probably still happening on P1, with liquid ligaments appearing, while computationally, these breakup is not happening. Therefore, P1 is not a representative window and is not used for determining the proper scale factor for the statistical distribution. P2 is a more representative window for characterizing the spray as it shows a completely atomized spray with only droplets passing through the window and no ligaments. Computational data, as mentioned, introduces the result of the complete breakup process therefore it represents better what is happening in this window and on P3. On Figure 9d a decrease of the peak of the most common value can be observed as the cross-flow is deflecting the smaller droplets, while the bigger ones with more inertia tend to follow the axial direction of the injector.

When it comes to P3, there is a big influence on the initial droplet distribution, as the greater the number of small droplets, the greater the number of droplets whose direction is

being bent towards the cross-flow direction. All the scale parameters used, specially $0.3d_n$ shows a distinct peak of very small droplets which are the ones influenced.

About the velocity distribution of Figure 9, there is a general trend for all the positions, which is a lack of dispersion of the computational results compared to the distributions of the experimental data is being validated against. There is little influence of the droplet distribution in P1 (Figures 9b and 9c) due to the proximity of this window to the nozzle exit. Once the spray penetrates further down into the domain, it starts to slow down. Initial distributions with smaller shape factor exchanges higher momentum with the air mass flow that incises perpendicularly, displacing the peak in the Y-Velocity (Figure 9f).

Some discrepancies can be visualized at Figure 9i. Computational results show two peaks, one at very low velocities and another at higher speeds, with respect to the only one peak that experimental data shows around to $25\,\mathrm{m\,s^{-1}}$. This is closely related to the diameter distribution at P3, Figure 9g. Such a number of small diameter droplets are highly drawn by the cross-flow in the X direction, having little Y-velocity component, translating into a peak of low Y-velocities and a very narrow distribution around a precise X-velocity value on Figure 9h. Discrepancies also arise from the impossibility of the DBI method to detect droplets below 21.7 µm due to the zoom and pix/mm limitations. These differences are also visible in other UWS computational sprays.[13,14]

As there are some doubts whether in P1 the primary atomization has already been completed due to being the reported breakup length of experiments[34] of the same order of magnitude of the distance between the mentioned window and the injection location in the experimental results, there would be no reason for comparing it with the computational data where droplets are introduced as the result of a complete primary atomization. In the end, the characteristic chosen is $0.3\mathrm{d_n}$ for the model scale parameter, as it better fits P2 and P3.

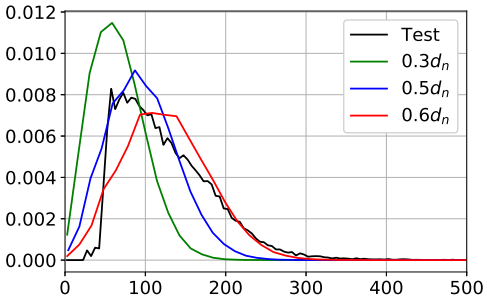

(a) P1 - Droplet Diameter

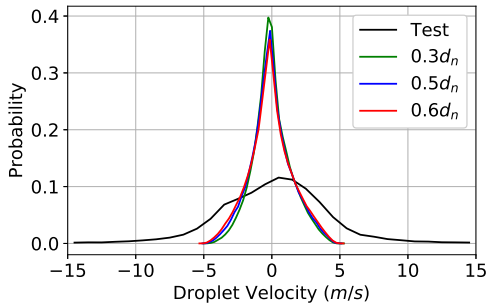

(b) P1 - X Velocity

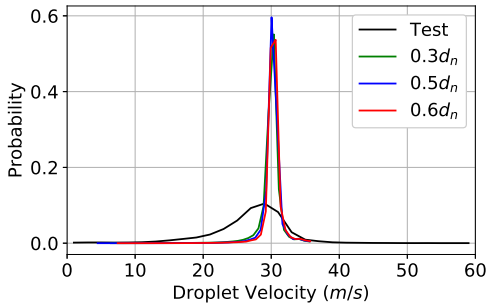

(c) P1 - Y Velocity

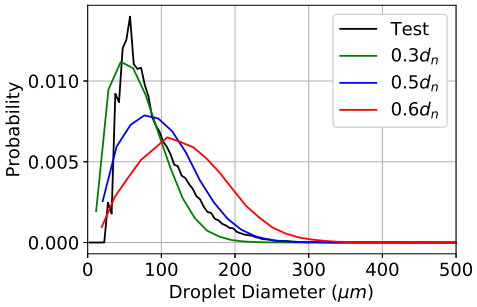

(d) P2 - Droplet Diameter

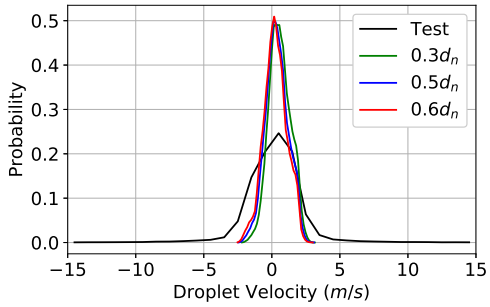

(e) P2 - X Velocity

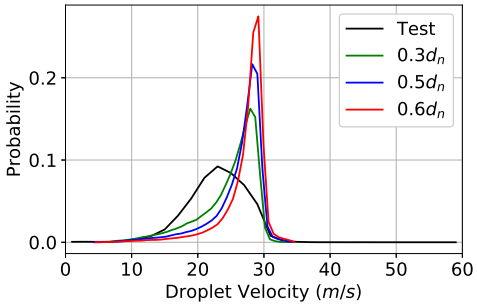

(f) P2 - Y Velocity

Figure 9: Comparison of probabilities of different shape parameters ($0.3d_n$, $0.5d_n$ and $0.6d_n$) with air at 350 °C and 40 kg h^{-1} of air cross mass flow rate at 6 bar of injection pressure with the corresponding experimental data.

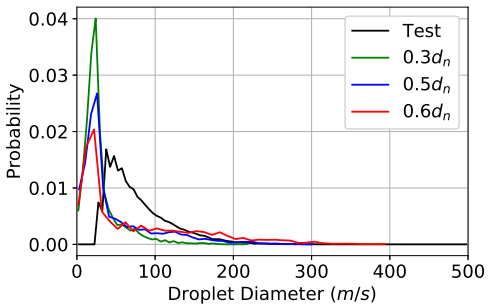

(g) P3 - Droplet Diameter

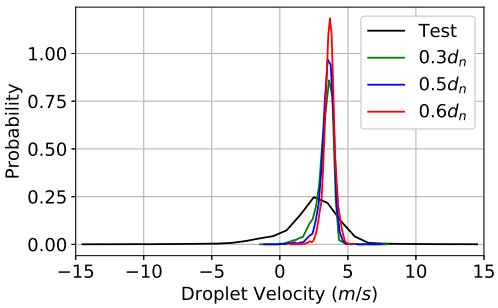

(h) P3 - X Velocity

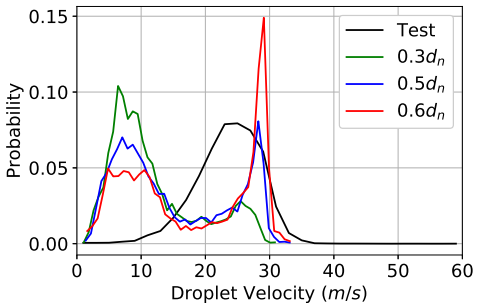

(i) P3 - Y Velocity

Figure 9: (Continued) Comparison of probabilities of different shape parameters ($0.3d_n$, $0.5d_n$ and $0.6d_n$) with air at 350 °C and 40 kg h^{-1} of air cross mass flow rate at 6 bar of injection pressure with the corresponding experimental data.

Penetration comparison

The evolution of the spray penetration for the case of 6 bar injection pressure has been compared against the experimental data (Figure 10). Experimentally, penetration is obtained as the furthest position of the spray contour obtained with the imaging.[22] The solid line of the previous figure represents the moving average of the penetration during 10 repetitions of the injection event, while the highlighted gray area represents the standard deviation of the corresponding 10 repetitions. Computationally, first the spray mass injected has been calculated, and then it has been multiplied by the liquid penetration fraction to obtain the penetrated spray mass from which the distance to the nozzle will be calculated. As the criteria followed for computing the penetration is to obtain the length in which the mass injected is the 99% of the total mass, the liquid penetration fraction has been set to 0.99. Except for the starting moments of the injection event, the CFD model predicts a more linear evolution of the penetration. Experiment expresses as well uniform velocity profile with a change of it at 1 ms, although there appears to be an under-prediction of it during the first millisecond After Start Of Injection (ASOI). The experimental data might be capturing effects of the dynamics of the needle as the sudden speed-up of the penetration curve could be associated to capturing droplets ahead of the main spray. The later deceleration at 1 ms ASOI then refers to the proper capturing of the main spray after those initial droplets have been washed away.

A second operating condition was used for validation purposes to ensure that the CFD model is capable of reproducing the physics correctly in all the injection pressure range. For it, a similar study was done with an injection pressure of 4 bar. Same behavior was found as in Figure 11, same tendency, and the results were as accurate as at the previous comparison (6 bar). Same acceleration and deceleration behavior was found which strengthens the isolated droplet detection hypothesis stated before, as due to the lower injection pressure, and therefore droplet velocities, these droplets bend their direction easier by the air flow rate. Accuracy metrics have been computed, Mean Absolute Error (MAE) and Root Mean

Square Error (RMSE), to assess the error between both curves at the two injection pressures simulated, and they are presented in Table 4.

Table 4: Error metrics between the experimental and computational penetration curves for two injection pressures, with air at 350 °C and a air flow rate of 40 kg/h.

Injection Pressure	MAE	RMSE
4 bar	3.53 mm	3.86 mm
6 bar	3.54 mm	4.12 mm

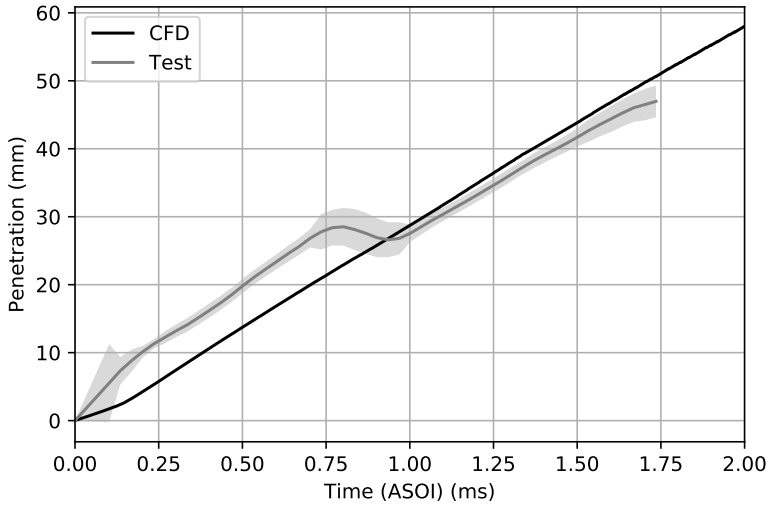

Figure 10: Spray penetration comparison between CFD and experimental results for 6 bar of injection pressure, 350 °C and 40 kg h^{-1} for the incoming air mass flow rate.

Injection pressure parametric study

Three injection pressures from within the working range of the dosing module were tested, 4 bar, 6 bar and 8 bar (gauge), with a chamber back-pressure of 1 bar (absolute). Cross flow temperature at 350 °C and a mass flow rate of 40 kg h^{-1} as in the validation case (Table 3). Results of the PDF of droplet size and velocities are included in Figure 12. Droplet diameter is very insensitive to injection pressure in the core region of the spray (Figures 12a and 12d). No differences appear, as shown by experimental dataset in Figure 13. In the outskirts,

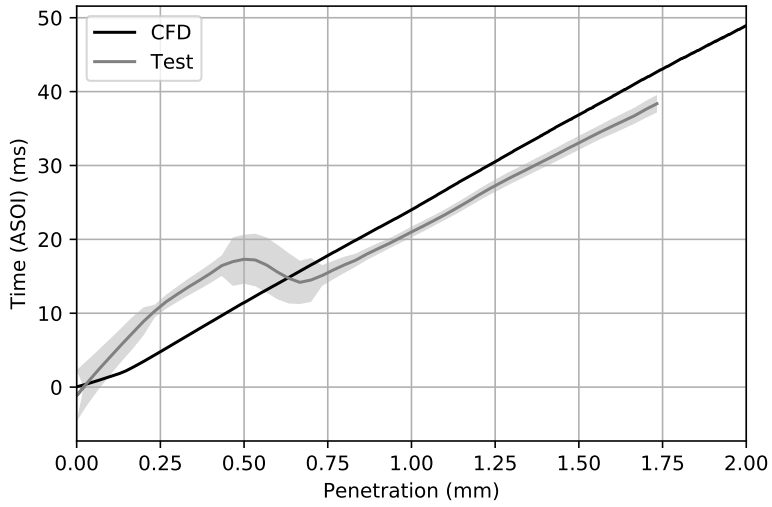

l

Figure 11: Spray penetration comparison between CFD and experimental results for 4 bar of injection pressure, 350 °C and 40 kg h^{-1} for the incoming air mass flow rate.

P3 (Figure 12g), some influence appears, with lower injection pressures there is a less pronounced peak associated with droplets of 25 µm. Lower injection pressures have associated a lower injection velocity, which translates into lower inertial forces on the droplet. This allows some droplets of bigger size to bend their direction due to the cross-direction mass flow. For the droplets with higher momentum it is more difficult to change their path towards the perpendicular direction, hence they do not appear through P3. Clear effect of the pressure is seen on the Y-velocity component of the droplets (Figure 12c), 8 bar corresponds approximately to 35 m s^{-1}, 6 bar to 31 m s^{-1} and 4 bar to 25 m s^{-1}. Figure 12c shows very skewed curves due to the proximity of P1 to the injector. As the spray starts to penetrate further into the domain, droplets start to suffer from drag which slows them down (Figure 12f). Velocity distribution for the X-axis shows values centered around the zero value as the X-origin is placed right in the injector location and the droplets follow the path and velocity dictated by the injection event.

Figure 14 shows the dependency of the droplet size in its transverse velocity (X-Axis), and with it reinforces the idea of which path those droplets follow depending on the diameter. It is shown how the very large droplets have almost none X-axis velocity or it is centered

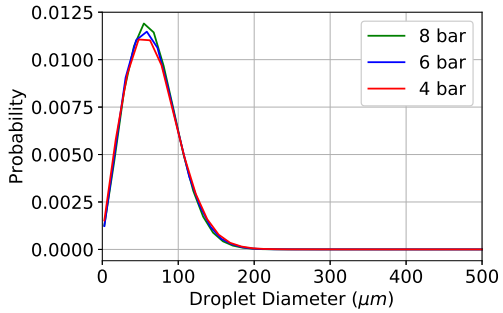

(a) P1 - Droplet Diameter

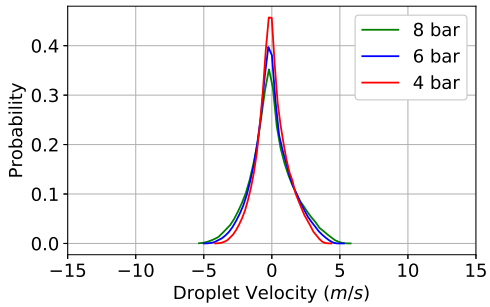

(b) P1 - X Velocity

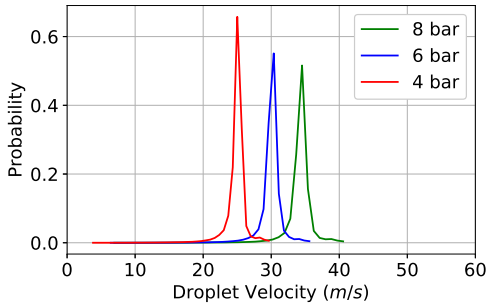

(c) P1 - Y Velocity

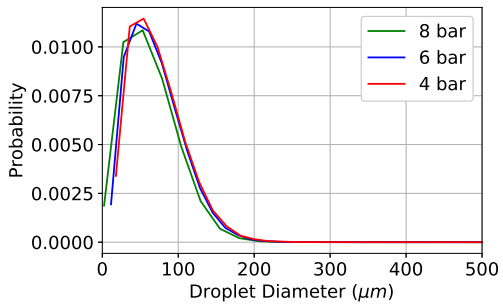

(d) P2 - Droplet Diameter

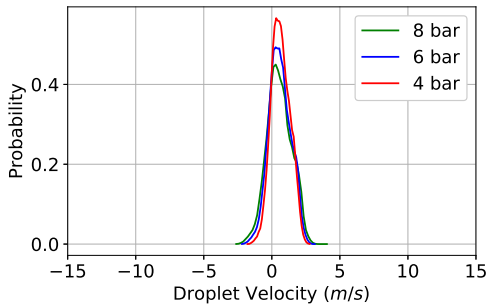

(e) P2 - X Velocity

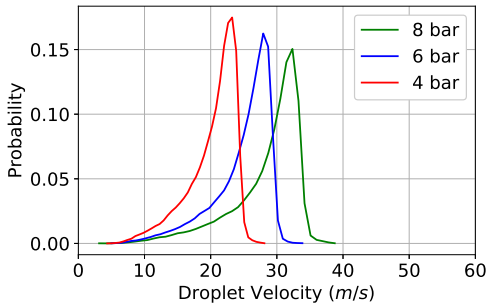

(f) P2 - Y Velocity

Figure 12: Probability density functions of the droplet diameters and its velocity for three injection pressures: 4 bar, 6 bar and 8 bar, with air at 350 °C and 40 kg/h of air flow rate.

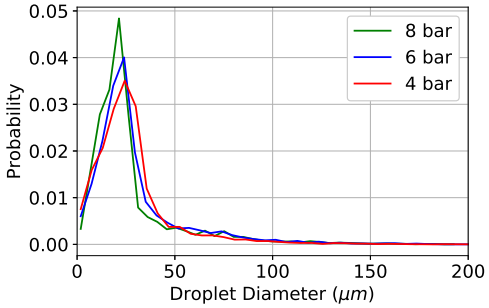

(g) P3 - Droplet Diameter

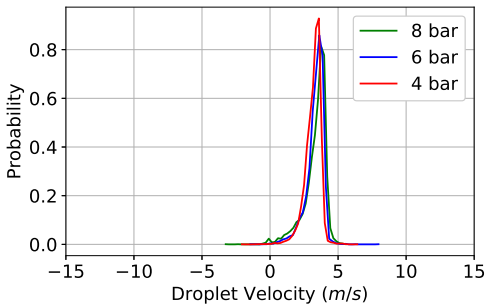

(h) P3 - X Velocity

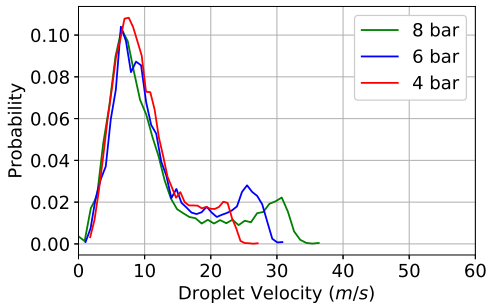

(i) P3 - Y Velocity

Figure 12: (Continued)Probability density functions of the droplet diameters and its velocity for three injection pressures: 4 bar, 6 bar and 8 bar, with air at 350 °C and 40 kg/h of air flow rate.

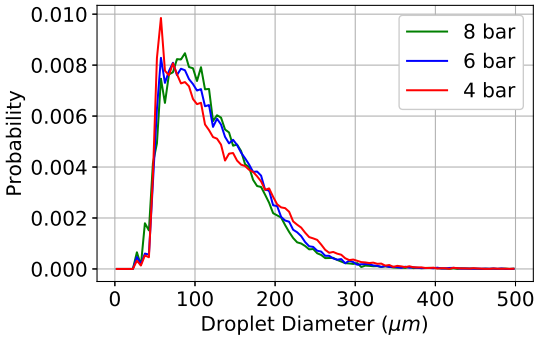

(a) P1 - Droplet Diameter

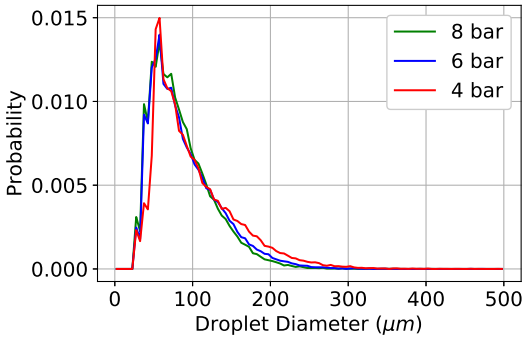

(b) P2 - Droplet Diameter

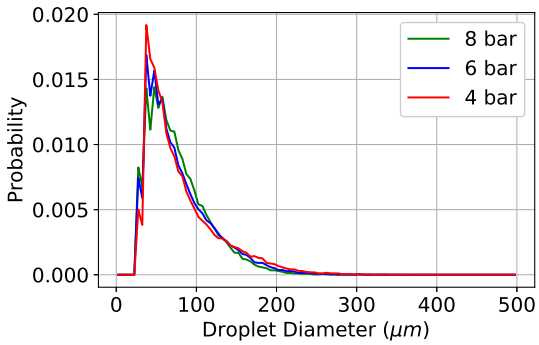

(c) P3 - Droplet Diameter

Figure 13: Probability density functions of the droplet diameters from experimental dataset at the three windows of interest at 4 bar, 6 bar and 8 bar of injection pressure, with air at 350 °C and 40 kg/h of air flow rate.

around that value. For droplets between 50 µm and 100 µm the velocity possibilities spreads wider, to both positive and negative values, more biased towards the positive ones due to the presence of the cross-flow. Droplets with diameters smaller than 50 µm show a trend towards positive velocities as the diameter goes even smaller. An exponential decay regression of the shape has been performed on the previous data to assess the tendencies just described. The resulting curve is also included in Figure 14.

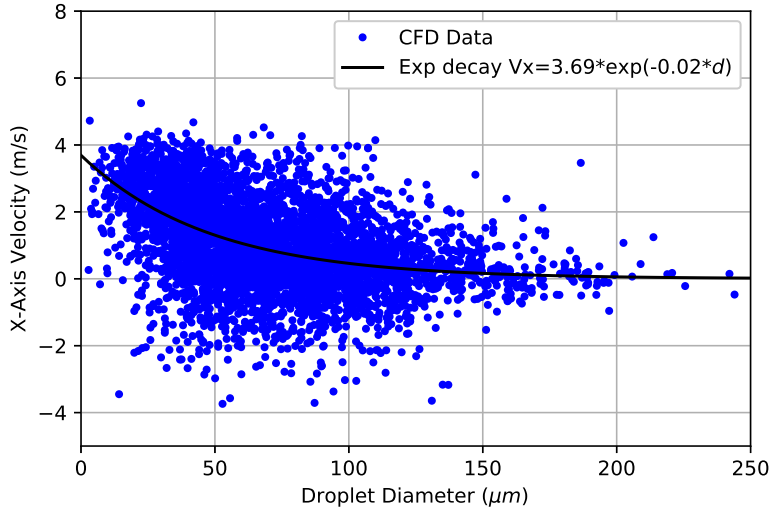

Figure 14: Droplet velocity on X-Direction against its diameter and associated regression curve for 6 bar of injection pressure, 350 °C of air and 40 kg h^{-1} of air mass flow rate.

Spray Angle

Angle is calculated based on the spray penetration, with the angle that forms the trapezium of the spray with the base formed by horizontal sections at 12% and 50% of the spray penetration.[22] For it, the angle formed with the spray axis has been computed both from the left and the right side of the spray (Figure 2) by identifying spray boundaries and obtaining a linear regression (Figure 15), and its result has been time-averaged. Droplets below 20 µm have been neglected in order to not suddenly distort the continuity of the angle coming from the nozzle exit.

The main results of the spray angle are summed up in Table 5. An influence of the injection pressure on the spray angle is found. Increasing the injection pressure results in a narrower angle. But, if the angle calculation procedure takes into account both sides of the spray separately, different effects are seen, and a considerable widening effect is observed for the right-hand side of the spray. This tendency is reasonable as the lower velocities derived from the lower injection pressures exchange momentum with the cross flow easier, changing the spray path towards the X-direction. The left-hand side of the spray widens with increasing injection pressure, but the magnitude of this effect is not as important as the effect on the right side of the spray.

Table 5: Simulation spray angle for three injection pressures, with air at 350 °C and a air flow rate of 40 kg/h.

	4 bar	6 bar	8 bar
Left side angle	6.0°	6.5°	7.0°
Right side angle	18.2°	14.8°	13°
Total angle	24.2°	21.3°	20.0°

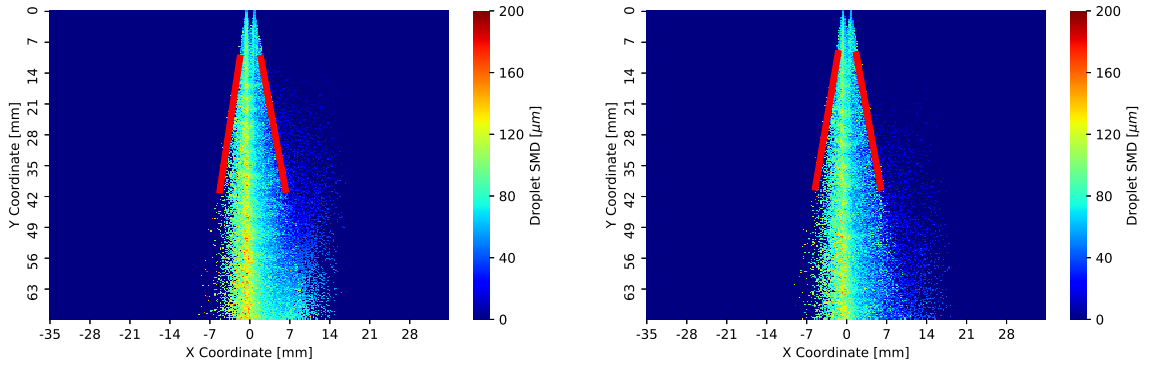

(a) 4 bar (b) 8 bar

Figure 15: Spray angle contour for two injection pressures: 4 bar and 8 bar, with air at 350 °C and an air mass flow rate of 40 kg/h.

Sauter Mean Diameter

The evolution of the spray droplet size of the UWS has been studied through a lateral projection of the droplet diameter. Results for a specific instant are included in Figure 16. The domain has been discretized into an uniform grid of 300x300 cells representing an X-Y plane, and the results at a simulation instant have been interpolated into it by checking if any droplet happened to fall within each cell without considering the Z coordinate. In that way, a Sauter Mean Diameter can be computed for each cell, having a lateral snapshot of the spray.

Two main zones of the spray can be extracted. First the spray core and secondly the outskirts of it, differentiated by distinct SMD, above and below 120 µm. The SMD spatial distribution of the core is linked with the injection pressure. With low injection pressures, droplets exit with lower momentum, and tend to acquire velocity in the X-direction dragged by the air flow. That effect removes small droplets from the core region into the periphery of the spray, leaving only large droplets there, increasing then the SMD. On the other hand, if the injected droplets have more inertia due to higher injection pressure, fewer small droplets are dragged out of the core, lowering the SMD. The increasing pressure confirms the trend, as with 4 bar of injection pressure, Figure 16a, the low inertia of the droplets helps the movement in the cross-flow direction, increasing the SMD of the spray core to droplets bigger than 120 µm, not because of coalescence, but mainly because the lack of presence of small sized droplets. At higher injection pressures, the SMD of the spray core is lower both in extension and in diameter, which is accompanied with less droplets following the cross-flow direction, which can also be seen in the right part of the spray outskirts. In addition, it allows a proper representation of the real contour of the injected UWS, which could not be seen in Figure 17.

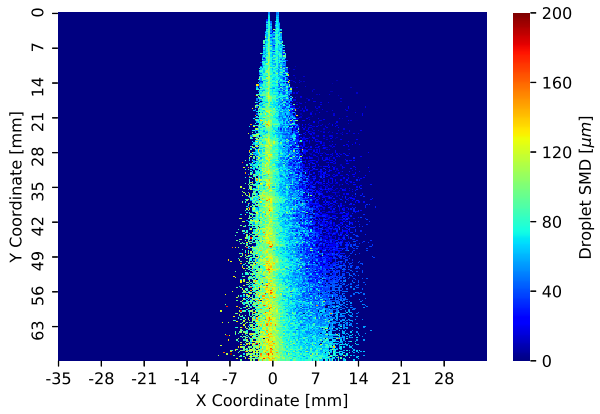

(a) 4 bar

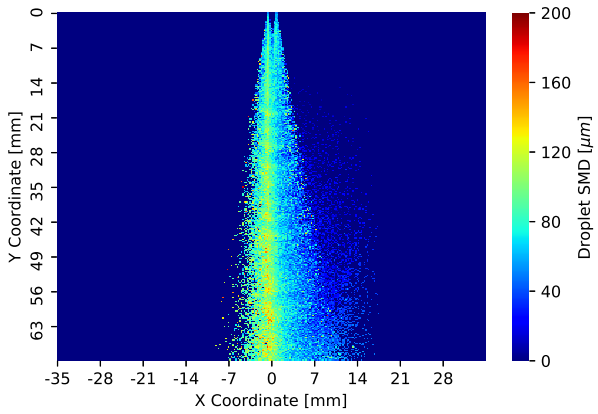

(b) 6 bar

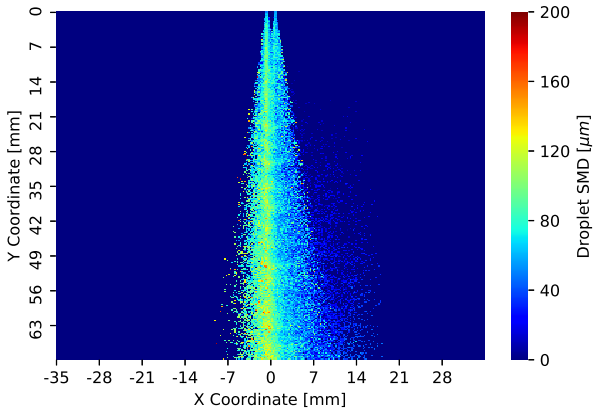

(c) 8 bar

Figure 16: Projection of the Sauter Mean Diameter of the UWS spray for three different injection pressures: 4 bar, 6 bar and 8 bar, with air at 350 °C and air mass flow rate of 40 kg/h.

Mass distribution

The spatial distribution of the spray's mass has been assessed by performing lateral projection of this parameter, by using the same grid created for the calculation of the Sauter Mean Diameter. For each of the cells created, the number of droplets whose X-Y coordinates fall into each cells is collected and its mass its added to the cell cumulative mass. Its results for the three injection pressures are included in Figure 17. The spray mass distribution is almost not affected by the pressure injection. It can be observed how mass is removed from the core to the outer layers of the spray due to the presence of the X-Direction air mass flow introduced, which displaces the smaller UWS droplets towards the domain exit. Discontinuities might be present as a consequence to the ROI profile oscillations (Figure 7), or due to that the droplet sizes are a consequence of a statistical distribution. Figure 17 allows to present how only the inner core of the injected fluid is visible with this representation, as the high diameter droplets remain in the mentioned core, while the droplets that are more prone to change their path towards the exit, the smaller diameter droplets that are in the cone outskirts, are almost negligible when it comes to mass representation. This plot, in addition to the information given by Figure 16, shows that most of the injected mass can be assigned to droplets bigger than 120 µm, while droplets lower than that are almost mass negligible.

Droplet Breakup

As commented in previous sections, the characteristics of the injection event, considering velocities, density and surface tension of AdBlue droplets, lead to a very low Weber number, meaning that any kind of droplet breakup mechanism is very unlikely to appear. Nonetheless, the Weber Number and the Reynolds Number have been computed for each droplet in the whole event, and its results have been included in Figure 18, taking the droplet diameter as the characteristic length, and the droplet surface tension suggested in the literature for this condition.[35] As it is seen, maximum Weber numbers are slightly above 1, far away from We =

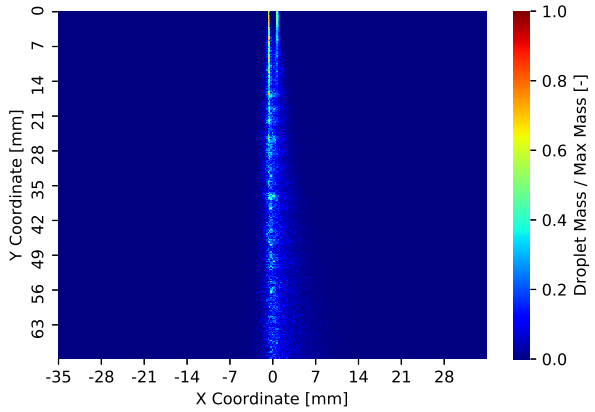

(a) 4 bar

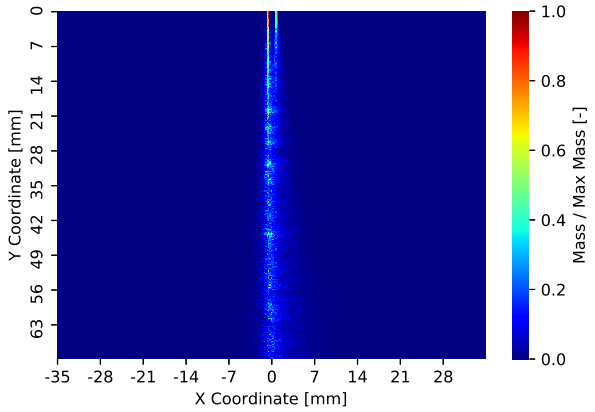

(b) 6 bar

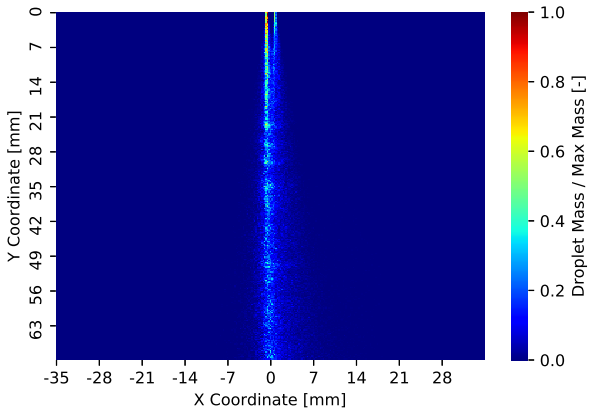

(c) 8 bar

Figure 17: Projection of the mass distribution of the UWS spray for three different injection pressures: 4 bar, 6 bar and 8 bar, with air at 350 °C and an air mass flow rate of 40 kg/h.

12 where droplet breakup should appear. Furthermore, from the outputs of the simulations it has been checked that not a single droplet had undergone a breakup process.

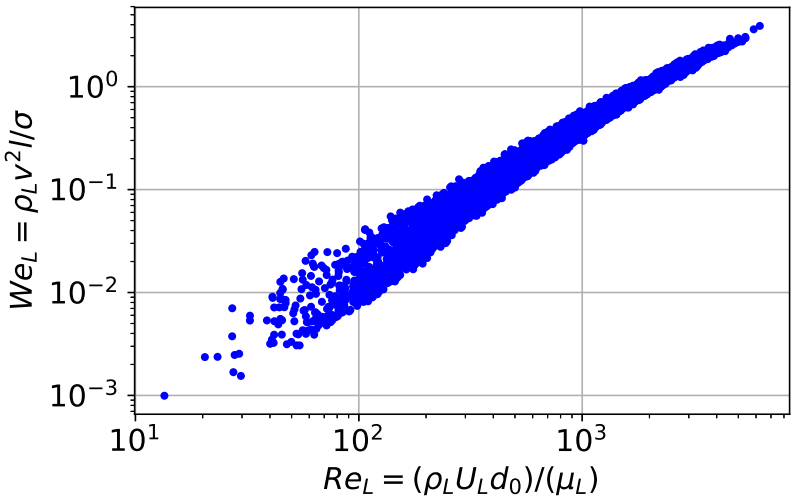

Figure 18: Droplet velocity on X-Direction against its diameter and associated regression curve for 6 bar of injection pressure, 350 °C of air and 40 kg h^{-1} of air mass flow rate.

Influence of cross-mass flow rate

After concluding that most of the UWS injected at nominal conditions was impacting the lower wall of the domain, it was found interesting to see the effects of increasing the mass flow to represent higher engine speed regimes and then the effect on the same injection event as before. For it, fixing the injection pressure to a value of 6 bar, the air mass flow was increased from its original value of 40 kg/h, to 200 kg/h and 400 kg/h, the maximum value the experimental facility can achieve for reproducing the gas flow at high engine regime.[36]

The PDF distributions have been performed on P2 and P3, but not on P1, because, due to the proximity to the injection location of this window, no difference has been seen on any of the variables of interest due to the little effect of the velocity of the incoming air.

Clear effects are seen on Figure 19. Figure 19a and Figure 19d translate its peak towards higher diameters, as well as the shapes are wider. First one is a consequence of sweeping

away from the spray core bigger droplets towards the X-direction, leaving only the droplets with higher mass and momentum which, as seen before, tend to keep more their initial injection direction. On P3 a similar analysis is to be made, with the exception of that there are no droplets below 50 µm, as those have bent its direction closer to the injection location (upper in the Y-axis). With higher air mass flow rates, only the droplets of around 80 µm of diameter can be found in this window, but droplets larger than that, which could be seen on P2 (around 150 µm), are not on P3 as they are following a trajectory closer to the injector axis. Due to the sharpness of the curves in P3, it can be stated that with 200 kg/h the droplets that appear in P3 are of 50 µm, and with 400 kg/h, 75 µm droplets are found. Particles bigger than those diameters are not bending their path that much, and the smaller particles already bent their path before reaching this particular window.

The X-velocity on P2 (Figure 19b) shows additional information on the large diameter droplets, since their values are not null anymore, shifting the peak value to $2.5\,\mathrm{m\,s^{-1}}$ in the case of 200 kg/h and $4\,\mathrm{m\,s^{-1}}$ with 400 kg/h. Y-velocity PDF shows a bell tightening tendency with increasing mass flow as most of the droplets are dragged uniformly by the air mass flow, having therefore the same kinetic characteristics. Droplets captured at P3, shows a sudden decrease of the peak value with the X-velocity and diameter, and a widening of the curve. The spreading of the velocity PDF is related to that wider range of droplet sizes and therefore different momentum exchange with the air. On Y-velocity, the two peak distribution disappears leaving a smooth one peak curve at 400 kg/h.

The study is as well complemented with projections of the mass and SMD in Figure 20 and Figure 21. Mass projections show a faster diffusion after the injection than the baseline case (Figure 17b). By analysing mass decay in the Y-axis, it can be obtained where the spray mass ratio value goes under 0.25 to detect the spray bending. It happens at 28 mm in the vertical direction for 200 kg/h (Figure 20a) and 15 mm in the vertical direction for 400 kg/h (Figure 20b), showing a faster diffusion for the highest air mass flow rate. The additional transverse mass flow helps scattering more the droplets, which implies a reduction

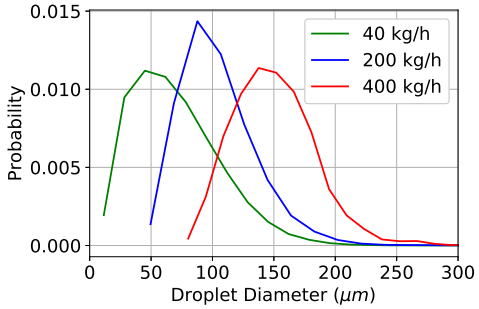

(a) P2 - Droplet Diameter

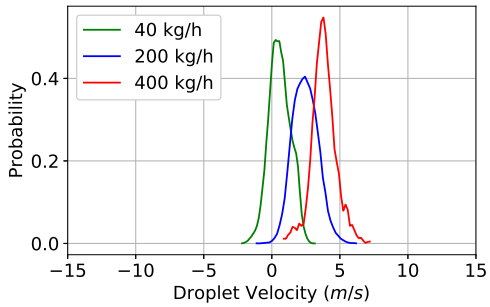

(b) P2 - X Velocity

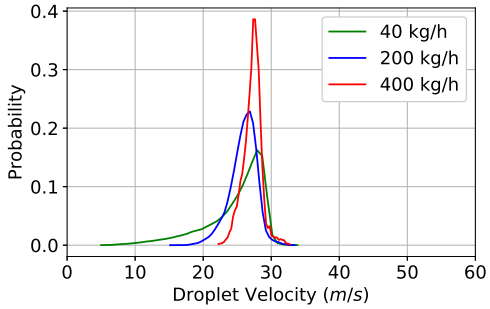

(c) P2 - Y Velocity

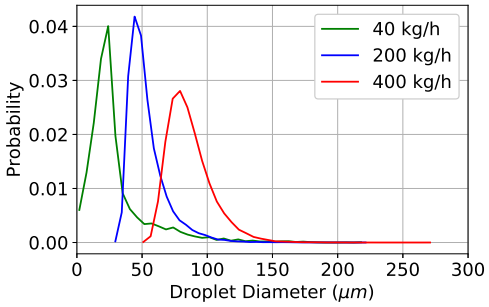

(d) P3 - Droplet Diameter

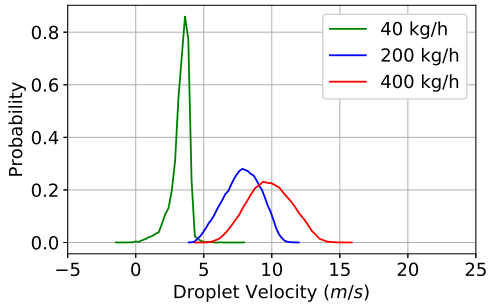

(e) P3 - X Velocity

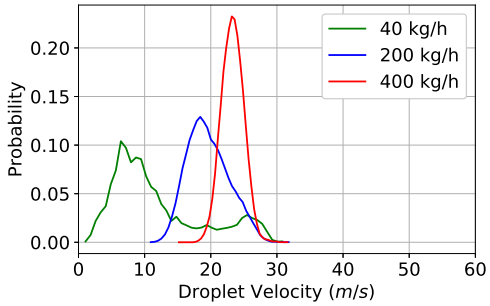

(f) P3 - Y Velocity

Figure 19: Probability density functions of the droplet diameters and its velocity for three cross-flow rates, 40 kg/h, 200 kg/h and 400 kg/h at an injection pressure of 6 bar and an air temperature of 350 °C.

on the observed mass for each of the windows. The SMD now is clearly discretized spatially as the droplets whose diameter is close to 200 µm are localized near to the injector axis, and progressively smaller droplets bend their path more and more until diameters smaller than 40 µm are almost aligned with the direction of the incoming air flow (Figure 21b).

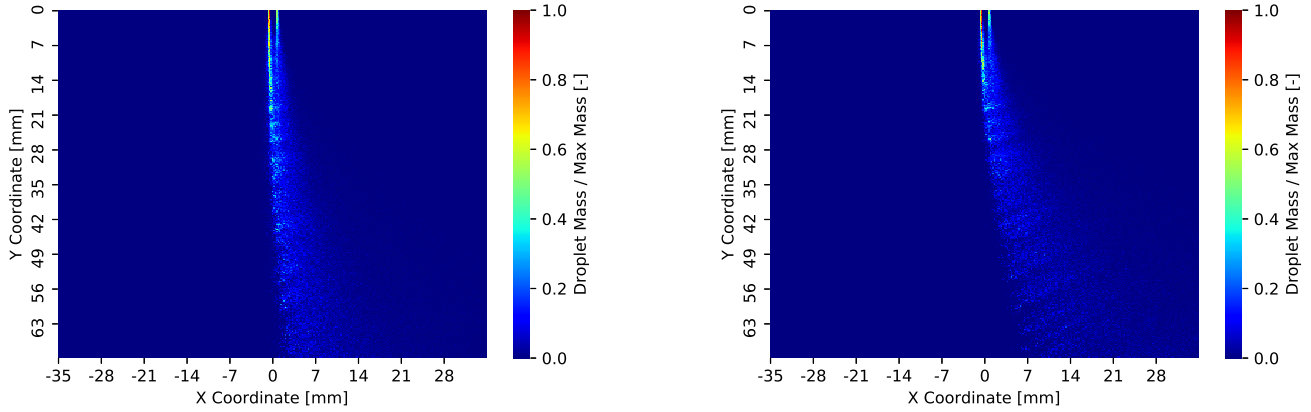

(a) 200 kg/h (b) 400 kg/h

Figure 20: Projection of the mass for 200 kg/h and 400 kg/h of an instant of the UWS injection at 6 bar, air at 350 °C.

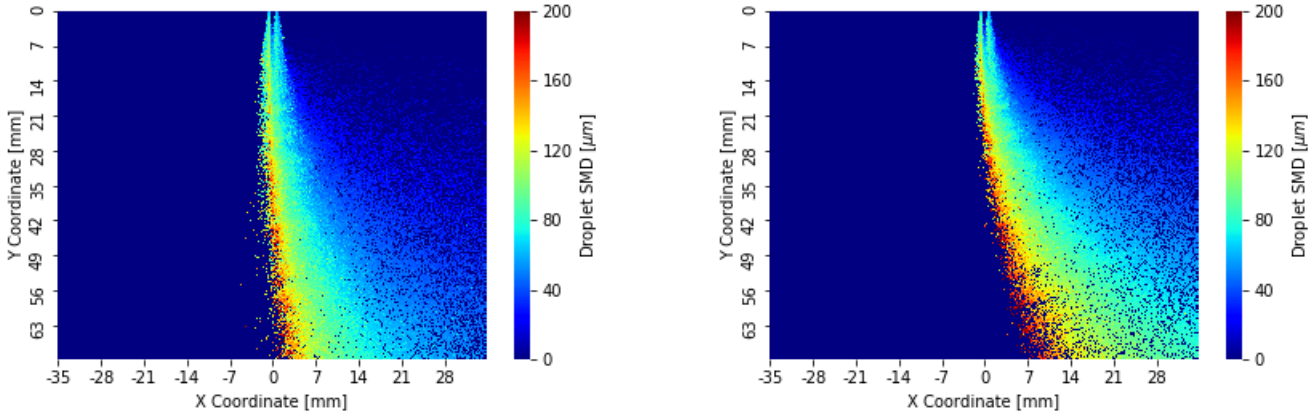

(a) 200 kg/h (b) 400 kg/h

Figure 21: Projection of the SMD for 200 kg/h and 400 kg/h of an instant of the UWS injection at 6 bar, air at 350 °C.

Conclusions

In the present work, the spray characteristics of an UWS spray have been assessed under typical working conditions. For it, a computational model has been created in CONVERGE v3.0 software and it has been validated against the experimental results coming from a DBI technique. Apart from it, the effect of the injection pressure has been assessed on the PDF curves as well as with the angle and SMD spatial distributions. Similar approach has been followed to predict the effect of an increase in the engine speed to realistic working conditions and the consequent rise in cross mass-flow. The following conclusions have been obtained:

- The low injection pressure for this application and the consequent low Weber number leads to the atomization prediction failure of the breakup models. A statistical distribution of droplet sizes needs to be introduced and a parametric study of the distribution needs to be made.

- The tightest distance between the injector inner walls is the driving parameter that characterizes the droplet size distribution along the spray as it shows to be the best characteristic length of the Rosin-Rammler distribution to fit the experimental data set. Spray penetration evolution was compared showing acceptable results as well, and the differences on the early part of the injection were attributed to non-steady of the injector needle.

- Pressure has no effect on the diameter distribution on any of the windows of interest. On the other side, lowering the injection pressure did have an effect on droplets inertia, which meant that the droplets bent more their path into the cross-flow direction. That change of direction was predominant in the droplets with diameters less than 50 µm.

- Large diameter droplets do follow the injector axis on the spray core, while the outskirts of the cone is made up from droplets of about 80 µm. Droplets under 50 µm of diameter leave the spray cone and move towards the exit of the domain, in the perpendicular

direction of the spray axis. Also, most of the injected mass corresponds to particles whose diameter is higher than 120 µm. This implies a worse droplet atomization of the spray core, and therefore a worse evaporation.

- Increasing the air flow rate decreases the amount of droplets that splash into the lower walls as it bends significantly the spray in the direction of the external flow as expected. In addition to it, helps distributing the droplets for an easier later evaporation, compared to the original 40 kg/h case where spots of accumulated mass were found in the spray projections. However, due to being dependent on the working regime of the engine, optimization can not be done with this variable.

Overall, the model created stands as a good tool to recreate UWS sprays prior to the SCR system to predict and analyse its flow behavior and try to optimize the injection process of low pressure injectors. Further studies could be associated with more realistic injection chamber geometries, or introducing Urea decomposing mechanics to analyse possible effects in the spray characteristics, as for the present work, both experimental and computational, hydrolysis and thermolysis were out of the scope.

Acknowledgement

This research has been partially funded by Spanish Ministerio de Ciencia, Innovación y Universidades through project RTI2018-099706-B-100. Additionally, the experimental hardware was purchased through FEDER and Generalitat Valenciana under project IDIFEDER/2018/037.

References

(1) Han, L.; Cai, S.; Gao, M.; Hasegawa, J. Y.; Wang, P.; Zhang, J.; Shi, L.; Zhang, D. Selective Catalytic Reduction of NOx with NH3 by Using Novel Catalysts: State of the

Art and Future Prospects. *Chemical Reviews* **2019**, *119*, 10916–10976.

(2) Reitz, R. D. et al. IJER editorial: The future of the internal combustion engine. *International Journal of Engine Research* **2019**, *21*, 146808741987799.

(3) Dammalapati, S.; Aghalayam, P.; Kaisare, N. Modeling the Effect of Nonuniformities from Urea Injection on SCR Performance Using CFD. *Industrial & Engineering Chemistry Research* **2019**, *58*, 20247–20258.

(4) Triantafyllopoulos, G.; Katsaounis, D.; Karamitros, D.; Ntziachristos, L.; Samaras, Z. Experimental assessment of the potential to decrease diesel NOx emissions beyond minimum requirements for Euro 6 Real Drive Emissions (RDE) compliance. *Science of the Total Environment* **2018**, *618*, 1400–1407.

(5) Inomata, Y.; Hata, S.; Mino, M.; Kiyonaga, E.; Morita, K.; Hikino, K.; Yoshida, K.; Kubota, H.; Toyao, T.; Shimizu, K. I.; Haruta, M.; Murayama, T. Bulk Vanadium Oxide versus Conventional V2O5/TiO2: NH3-SCR Catalysts Working at a Low Temperature below 150 °c. *ACS Catalysis* **2019**, *9*, 9327–9331.

(6) Xue, Z.; Du, X.; Rac, V.; Rakic, V.; Wang, X.; Chen, Y.; Xiang, J.; Song, L. Partial Oxidation of NO by H2O2 and afterward Reduction by NH3-Selective Catalytic Reduction: An Efficient Method for NO Removal. *Industrial & Engineering Chemistry Research* **2020**, *59*, 9393–9397.

(7) Nuguid, R. J. G.; Ferri, D.; Marberger, A.; Nachtegaal, M.; Kröcher, O. Modulated Excitation Raman Spectroscopy of V2O5/TiO2: Mechanistic Insights into the Selective Catalytic Reduction of NO with NH3. *ACS Catalysis* **2019**, *9*, 6814–6820.

(8) Yim, S. D.; Kim, S. J.; Baik, J. H.; Nam, I. S.; Mok, Y. S.; Lee, J. H.; Cho, B. K.; Oh, S. H. Decomposition of urea into NH3 for the SCR process. *Industrial & Engineering Chemistry Research* **2004**, *43*, 4856–4863.

(9) Zheng, G.; Fila, A.; Kotrba, A.; Floyd, R. Investigation of urea deposits in urea SCR systems for medium and heavy duty trucks. *SAE Technical Papers* **2010**, *2010-01-19*.

(10) Strots, V. O.; Santhanam, S.; Adelman, B. J.; Griffin, G. A.; Derybowski, E. M. Deposit formation in urea-scr systems. *SAE International Journal of Fuels and Lubricants* **2010**, *2*, 283–289.

(11) Abu-Ramadan, E.; Saha, K.; Li, X. Modeling of the injection and decomposition processes of urea-water-solution spray in automotive SCR systems. *SAE 2011 World Congress and Exhibition* **2011**, *2011-01-13*.

(12) Sowman, J.; Laila, D. S.; Fussey, P.; Truscott, A.; Cruden, A. J. Nonlinear model predictive control applied to multivariable thermal and chemical control of selective catalytic reduction aftertreatment. *International Journal of Engine Research* **2019**, *20*, 1017–1024.

(13) Varna, A.; Boulouchos, K.; Spiteri, A.; Dimopoulos Eggenschwiler, P.; Wright, Y. M. Numerical Modelling and Experimental Characterization of a Pressure-Assisted Multi-Stream Injector for SCR Exhaust Gas After-Treatment. *SAE International Journal of Engines* **2014**, *7*, 2012–2021.

(14) Varna, A.; Spiteri, A. C.; Wright, Y. M.; Dimopoulos Eggenschwiler, P.; Boulouchos, K. Experimental and numerical assessment of impingement and mixing of urea-water sprays for nitric oxide reduction in diesel exhaust. *Applied Energy* **2015**, *157*, 824–837.

(15) Van Vuuren, N.; Brizi, G.; Buitoni, G.; Postrioti, L.; Ungaro, C. Experimental analysis of the urea-water solution temperature effect on the spray characteristics in SCR systems. *SAE Technical Papers* **2015**, *2015-24-25*.

(16) Van Vuuren, N.; Brizi, G.; Buitoni, G.; Postrioti, L.; Ungaro, C. AUS-32 Injector Spray Imaging on Hot Air Flow Bench. *SAE Technical Papers* **2015**, *2015-01-10*.

(17) Kapusta, Ł. J.; Sutkowski, M.; Rogóż Rafałand Zommara, M.; Teodorczyk, A. Characteristics of water and urea-water solution sprays. *Catalysts* **2019**, *9*, 750.

(18) Rogóż, R.; Łukasz Jan Kapusta,; Bachanek, J.; Vankan, J.; Teodorczyk, A. Improved urea-water solution spray model for simulations of selective catalytic reduction systems. *Renewable and Sustainable Energy Reviews* **2020**, *120*, 109616.

(19) Bebe, J. E.; Andersen, K. S. Validation of a CFD Spray Model Based on Spray Nozzle Characteristics. WCX™ 17: SAE World Congress Experience. 2017.

(20) Vojtisek-Lom, M.; Kotek, M. Estimation of Engine Intake Air Mass Flow using a generic Speed-Density method. *Journal of Middle European Construction and Design of Cars* **2014**, *12*.

(21) Payri, R.; Bracho, G.; Gimeno, J.; Moreno, A. Investigation of the urea-water solution atomization process in engine exhaust-like conditions. *Experimental Thermal and Fluid Science* **2019**, *108*, 75–84.

(22) Payri, R.; Bracho, G.; Gimeno, J.; Moreno, A. Spray characterization of the urea-water solution (UWS) injected in a hot air stream analogous to SCR system operating conditions. *SAE Technical Papers* **2019**, *2019-01-07*.

(23) Sechenyh, V.; Duke, D. J.; Swantek, A. B.; Matusik, K. E.; Kastengren, A. L.; Powell, C. F.; Viera, A.; Payri, R.; Crua, C. Quantitative analysis of dribble volumes and rates using three-dimensional reconstruction of X-ray and diffused back-illumination images of diesel sprays. *International Journal of Engine Research* **2019**, *21*, 43–54.

(24) BASF, AdBlue®Technical Leaflet. 2006; `https://www.gabriels.be/sites/gabriels/files/pdf/technische_fiche_adblue-_engels.pdf`.

(25) Senecal, P. K.; Pomraning, E.; Richards, K. J.; Som, S. Grid-Convergent Spray Models for Internal Combustion Engine CFD Simulations. 2012.

(26) Patterson, M. A.; Reitz, R. D. Modeling the Effects of Fuel Spray Characteristics on Diesel Engine Combustion and Emission. SAE Technical Paper. 1998.

(27) Schmidt, D. P.; Rutland, C. J. A New Droplet Collision Algorithm. *Journal of Computational Physics* **2000**, *164*, 62–80.

(28) Chiang, C. H.; Raju, M. S.; Sirignano, W. A. Numerical analysis of convecting, vaporizing fuel droplet with variable properties. *International Journal of Heat and Mass Transfer* **1992**, *35*, 1307–1324.

(29) Payri, R.; Gimeno, J.; Martí-Aldaraví, P.; Viera, A. Measurements of the mass allocation for multiple injection strategies using the rate of injection and momentum flux signals. *International Journal of Engine Research* **2020**, 1–16.

(30) Payri, R.; Salvador, F. J.; Gimeno, J.; Montiel, T. Aging of a Multi-Hole Diesel Injector and Its Effect on the Rate of Injection. *SAE Technical Paper* **2020**, 1–9.

(31) Benjamin, S. F.; Roberts, C. A. In *Fuel Systems for IC Engines*; IMechE,, Ed.; Woodhead Publishing: Cambridge, UK, 2012; pp 43–60.

(32) Gapin, A.; Demoulin, F.; Dumouchel, C.; Pajot, K.; Patte-Rouland, B.; Réveillon, J. Development of an Initial Drop-Size Distribution Model and Introduction in a CFD Code to Predict Spray Evolution Computational Techniques for Multiphase Flows. 7th International Conference on Multiphase Flow - ICMF. Tampa, FL USA, 2010.

(33) Lefebvre, A. H.; McDonell, V. G. *Combustion: An International Series*, 2nd ed.; Press, CRC: Boca Raton, FL, 2017; pp 17–69.

(34) Senthilkumar, P.; Shamit, B.; Anand, T. Breakup Length of Urea Water Solution Jet in a Hot Cross Flow. 28th Conference on Liquid Atomization and Spray Systems - ILASS. Valencia, Spain, 2017.

(35) Halonen, S.; Kangas, T.; Haataja, M.; Lassi, U. Urea-Water-Solution Properties: Density, Viscosity, and Surface Tension in an Under-Saturated Solution. *Emission Control Science and Technology* **2017**, *3*, 161–170.

(36) Heywood, J. B. *Internal combustion engine fundamentals*, 2nd ed.; McGraw-Hill,: New York, NY, 2018; pp 42–57.

Payri, R., Bracho, G., Martí-Aldaraví, P., & Marco-Gimeno, J. (2020). Computational Study of Urea–Water Solution Sprays for the Analysis of the Injection Process in SCR-like Conditions. Industrial & Engineering Chemistry Research, 59(41), 18659–18673. https://doi.org/10.1021/acs.iecr.0c02494

Graphical TOC Entry